JOURNAL OF SPACECRAFT AND ROCKETS
Vol. 41, No. 4, July–August 2004

Aerogravity-Assist Maneuvering of a Tethered Satellite System

Michael D. Jokic* and W. J. T. Daniel†
University of Queensland, Brisbane, Queensland 4072, Australia

Two new implementations of a tethered satellite system to provide aeroassist during a planetary flyby are investigated. In each mission scenario the interaction of the Martian atmosphere with an aerodynamic lifting surface, which is tethered to an orbiter, is used to perturb the flight path of the system. The aerodynamic forces generated by interacting with the atmosphere augment the gravity assist provided by the planet. In the first aerogravity-assist maneuver the tethered satellite system has congruent post- and preflyby configurations. The second scenario, which is referred to as a dual-destination mission, involves the system mass being separated during the flyby. Both of these aerogravity-assist maneuvers are shown to facilitate significant, propellant-free velocity changes.

Nomenclature

A	=	exposed wedge surface area, m^2
$\boldsymbol{a}$	=	acceleration vector, m/s^2
C_d	=	drag coefficient
$\boldsymbol{c}_1, \boldsymbol{c}_2, \boldsymbol{c}_3$	=	orthogonal unit vectors
$\boldsymbol{F}$	=	force vector, N
H	=	atmospheric density scale height, m
$\boldsymbol{H}$	=	angular momentum vector, kg · m^2/s
H_r	=	atmospheric density reference height, m
I	=	moment of inertia, kg · m^2
l	=	length, m
$\boldsymbol{M}$	=	moment vector, N · m
m	=	mass, kg
P	=	atmospheric pressure, kPa
$\boldsymbol{R}$	=	radial vector from the center of Mars, m
S	=	frontal surface area, m^2
$\boldsymbol{V}$	=	velocity vector, m/s
α	=	probe angle of attack, rad
β	=	tether orientation angle measured from the vertical, rad
γ	=	wedge angle, rad
δ	=	deflection angle of the freestream, rad
θ	=	angular displacement of the center of mass about the planet's center, rad
μ	=	planetary gravitational constant, m^3/s^2
ρ	=	atmospheric density, kg/m^3
Ω	=	angular speed of the atmosphere, rad/s

Subscripts

cm	=	center of mass
d	=	drag
g	=	gravity
i	=	tether element
k	=	system mass element
l	=	lift
o	=	orbiter
p	=	probe
pl	=	planet property
ref	=	reference value
t	=	tether
∞	=	freestream conditions

Received 23 September 2002; revision received 16 March 2003; accepted for publication 15 May 2003.

*Ph.D. Candidate, Division of Mechanical Engineering. Member AIAA.
†Lecturer, Division of Mechanical Engineering.

Introduction

THE range of applications previously proposed for tethered satellite systems is considerable. A significant proportion of the research into these applications requires the tethered satellite system to interact with an atmosphere. Some of the mission proposals include using tethered satellite systems to conduct upper atmospheric research,[1] collect dust from the Martian atmosphere,[2,3] and act as a test facility for hypervelocity vehicles.[4] Bogar et al.[5] consider the implementation of a tethered vehicle as the upper stage of a launch system. This tether application requires the system to interact with Earth's atmosphere while transferring a payload into orbit. The potential benefits of these concepts represent a strong motivation for developing detailed models that describe the behavior of tethered satellite systems interacting with an atmosphere.

Researchers implement several modeling techniques to represent the inherently complex dynamics of tethered systems in space. Various authors[6,7] successfully demonstrate mission scenarios by treating the tether as a rigid rod with finite mass. Breakwell and Gearhhart[8] take the propitious approach of modeling a space tether by treating the system as a rigid rod without mass. Many researchers, however, model the tether as a single flexible body.[9–11] Alternative approaches presented in the literature treat the tether as a system of interconnected rigid masses. Specifically, these schemes are a lumped mass, or bead-type model,[12] and an approach that represents a tether as a series of interconnected rigid rods.[13]

A notable amount of research focuses on developing models of tethered systems that interact with an atmosphere. No and Cochran[14,15] and Bae et al.[16] develop models for the dynamics of systems consisting of a flight vehicle tethered to an orbiting mass. In line with this research, Biswell and Puig-Suari[17] investigate the use of a lifting probe tethered to an orbiting mass as a control actuator. Warnock and Cochran[18] account for the variation in flow regimes, in which a tethered satellite system might operate. In their work the drag acting on the tether is determined using aerodynamic coefficients that are dependent on the rarefaction of the flow as can be characterized by its Knudsen number.

Aerobraking, aerocapture, and aerogravity-assist maneuvering techniques can be performed using tethered systems. However, only the aerobraking and aerocapture maneuvers are considered rigorously in the literature. Longuski and Puig-Suari[6] successfully demonstrate the implementation of aerobraking and aerocapture maneuvers at Mars using a tethered satellite system with a dumbbell configuration. This work is extended by considering locations throughout the solar system[19] and optimized to minimize the tether mass.[20] Biswell[21] outlines a three-dimensional hinged-rod model of an elastic tether to predict the behavior and performance of the aerocapture maneuver in detail.

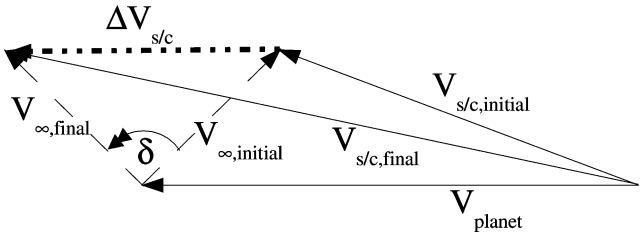

Fig. 1 Vector diagram for a gravity-assist maneuver.

Figure 1 depicts the change in velocity achieved during a typical gravity-assist maneuver in which gravitational forces are used to change the spacecraft's heliocentric (sun-centered) velocity. During the flyby, the spacecraft's velocity relative to the planet $\boldsymbol{V}_\infty$ is rotated δ by the influence of gravitational forces. The end result of the flyby is that the final heliocentric velocity $\boldsymbol{V}_{\mathrm{s/c,final}}$ is different from the velocity before the maneuver $\boldsymbol{V}_{\mathrm{s/c,initial}}$. By interacting with the atmosphere of a planet, the change in heliocentric velocity $\Delta V_{\mathrm{s/c}}$ achieved by gravitational forces can be increased. A maneuver in which both aerodynamic and gravitational forces are used to change the heliocentric velocity of a vehicle is known as an aerogravity-assist (AGA) maneuver. The many benefits afforded to interplanetary missions by aerogravity-assist maneuvers make them the focus of a significant amount of research.[22–24] Randolph and McRonald[25] demonstrate the potential to improve launch date opportunities and reduce travel times through engaging in aerogravity-assist maneuvers. Recent research, however, focuses on the scenario wherein the entire system's mass is incorporated into a waverider, which has the benefit of a high lift-to-drag ratio. This scenario restricts the aerodynamic design of the lifting body,[26] is extremely sensitive to trajectory errors, and commits the entire mission package to entering an uncertain environment. In relation to these issues, a tethered configuration offers important benefits.

This investigation represents a synthesis of research into tethered satellite systems (TSS) and AGA maneuvers. Several important benefits are availed to missions that employ the proposed TSS-AGA concept. The interaction of the tethered system with a planet's atmosphere permits propellant-free adjustment of the system's velocity. In addition, the tethered configuration facilitates part of the system mass being maintained outside the sensible atmosphere and might allow system adjustment to accommodate trajectory errors and environmental effects. The purpose of this work is to demonstrate two aerogravity-assist maneuvers using a tethered satellite system and to identify some of the associated technical issues and design variables. Several flybys of Mars, which exemplify the two distinct mission scenarios, are simulated using a rigid-rod model.

System Description

A system consisting of an idealized aerodynamic surface connected by a thin tether to a primary orbiting mass is adopted in this investigation. Figure 2 depicts the geometry and nomenclature describing the tethered system during a planetary flyby. The idealized aerodynamic surface is referred to as the atmospheric probe and the primary orbiting mass as the orbiter. The investigation by Longuski and Puig-Suari[6] is followed in developing the equations of motion.

To simplify the analysis of the system behavior during aerogravity-assist maneuvers, several assumptions are made. The orbiter mass m_o and probe mass m_p are assumed to be concentrated at a point. In addition, the tethered system is propagated in an equatorial orbit to justify modeling in a single plane. As the atmosphere is assumed to rotate with the planet, an equatorial orbit ensures that there are no significant crosswinds to cause out-of-plane aerodynamic forces. A rotating reference frame, which is shown in Fig. 2, facilitates the derivation of the system's equations of motion.

The tether is modeled as an inextensible series of nodes, which remain collinear during the system's motion. A nodal representation is adopted to reduce the computational effort demonstrated previously for a rigid-rod calculation.[17] The rigid, or collinear, behavior of the adopted tether model is unlike typical lumped-mass models, which

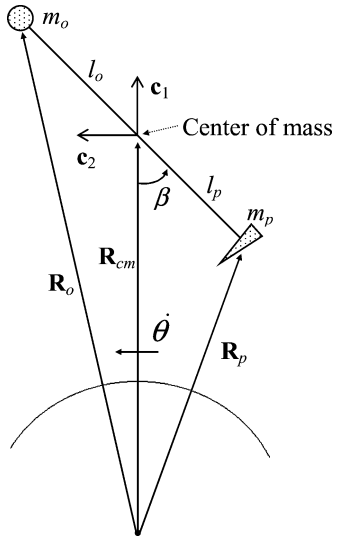

Fig. 2 System configuration.

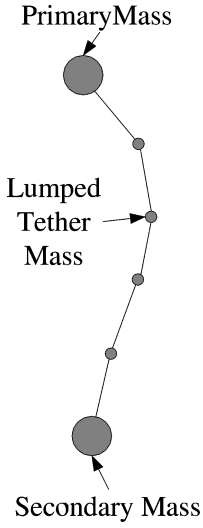

Fig. 3 Deformation of a typical lumped-mass tether model.

allow the tether to deform. Figure 3 demonstrates the deformation of a tether permitted by a typical lumped-mass model.

Newton's law is used to develop the translation equations of motion for the system's center of mass. This is expressed as

$$\boldsymbol{F} = m\boldsymbol{a}_{\mathrm{cm}} \tag{1}$$

The acceleration can be expressed relative to the center of the planet using[27]

$$\boldsymbol{a}_{\mathrm{cm}} = \left(\ddot{R}_{\mathrm{cm}} - R_{\mathrm{cm}}\dot{\theta}^2\right)\boldsymbol{c}_1 + \left(R_{\mathrm{cm}}\ddot{\theta} + 2\dot{R}_{\mathrm{cm}}\dot{\theta}\right)\boldsymbol{c}_2 \tag{2}$$

Moments acting on the tether system about its center of mass are found from Euler's law, which is expressed as

$$\boldsymbol{M} = \frac{\mathrm{d}\boldsymbol{H}_{\mathrm{cm}}}{\mathrm{d}t} \tag{3}$$

where the angular momentum is defined as[27]

$$\boldsymbol{H}_{\mathrm{cm}} = I_{\mathrm{cm}}\boldsymbol{\omega} \tag{4}$$

For the tethered system modeled in this investigation, the time derivative of the angular momentum is expressed as[6]

$$\frac{\mathrm{d}\boldsymbol{H}_{\mathrm{cm}}}{\mathrm{d}t} = \left[m_p l_p^2 + m_o l_o^2 + \frac{m_t}{(3l)\left(l_o^3 + l_p^3\right)}\right](\ddot{\beta} + \ddot{\theta})\boldsymbol{c}_3 \tag{5}$$

Gravitational Forces

The Newtonian inverse square model is adopted for determining the gravitational forces. For the assumed spherical planetoid the gravitational forces acting on the orbiter and probe are defined as

$$\boldsymbol{F}_{\text{go}} = -\mu m_o \boldsymbol{R}_o \big/ R_o^3 \tag{6}$$

$$\boldsymbol{F}_{\text{gp}} = -\mu m_p \boldsymbol{R}_p \big/ R_p^3 \tag{7}$$

The corresponding position vectors are

$$\boldsymbol{R}_o = (R_{\text{cm}} + l_o \cos\beta)\boldsymbol{c}_1 + l_o \sin\beta \boldsymbol{c}_2 \tag{8}$$

$$\boldsymbol{R}_p = (R_{\text{cm}} - l_p \cos\beta)\boldsymbol{c}_1 - l_p \sin\beta \boldsymbol{c}_2 \tag{9}$$

Determining the torques acting on the tethered system requires the calculation of the lever arm from the system's center of mass to each of the system point masses. The lever arm for a point mass located along the tether at a length l_k from the probe is given by

$$f(l_k) = l_k - l_p \tag{10}$$

Equation (10) also gives the sign of the moment contribution. Subsequently, the gravitational torque contributions for the orbiter and probe point masses are determined from

$$\boldsymbol{M}_{\text{go}} = (\boldsymbol{R}_o - \boldsymbol{R}_{\text{cm}}) \times \boldsymbol{F}_{\text{go}} = f(l_o)\mu m_o R_{\text{cm}} \sin\beta \big/ R_o^3 \boldsymbol{c}_3 \tag{11}$$

$$\boldsymbol{M}_{\text{gp}} = (\boldsymbol{R}_p - \boldsymbol{R}_{\text{cm}}) \times \boldsymbol{F}_{\text{gp}} = f(l_p)\mu m_p R_{\text{cm}} \sin\beta \big/ R_p^3 \boldsymbol{c}_3 \tag{12}$$

respectively.

As the tether is represented as a series of nodes, the gravitational force acting on the tether is the sum of their individual contributions. The total gravitational force acting on the tether can be represented as

$$\boldsymbol{F}_{\text{gt}} = \sum \boldsymbol{F}_{\text{gi}} = \sum -\mu m_i \boldsymbol{R}_i \big/ R_i^3 \tag{13}$$

The position vector of a node is defined as

$$\boldsymbol{R}_i = [R_{\text{cm}} + f(l_i)\cos\beta]\boldsymbol{c}_1 + f(l_i)\sin\beta \boldsymbol{c}_2 \tag{14}$$

where $f(l_i)$ is determined using Eq. (10). The total moment generated by the gravitational forces is also determined from the sum of the contributions of the individual point masses, which is written as

$$\begin{aligned}\boldsymbol{M}_{\text{gt}} &= \sum (\boldsymbol{R}_i - \boldsymbol{R}_{\text{cm}}) \times \boldsymbol{F}_{\text{gi}} \\ &= \sum f(l_i)\mu m_i R_{\text{cm}} \sin\beta \big/ R_i^3 \boldsymbol{c}_3\end{aligned} \tag{15}$$

Aerodynamic Forces

The aerodynamic forces are determined based upon the assumption that the atmosphere rotates with the planet. Exponential models for the density and pressure distributions in the atmosphere are adopted. For a body at radius R_k, the density is determined by

$$\rho_k = \rho_{\text{ref}} \exp[(H_r - R_k + R_{\text{pl}})/H] \tag{16}$$

and the pressure using

$$P_k = 0.699 \exp\left[-9 \times 10^{-5}(R_k - R_{\text{pl}})\right] \tag{17}$$

Orbiter and Tether Drag

The aerodynamic drag acting on the orbiter and tether is assumed to follow

$$\boldsymbol{F}_d = -\tfrac{1}{2}\rho C_d S V \boldsymbol{V} \tag{18}$$

Hence, the equation for the drag force acting on the orbiter is

$$\boldsymbol{F}_{\text{do}} = -\tfrac{1}{2}\rho_o C_{\text{do}} S_o V_o \boldsymbol{V}_o \tag{19}$$

where the velocity of the orbiter relative to the atmosphere is defined as

$$\begin{aligned}\boldsymbol{V}_o = {} & [\dot{R}_{\text{cm}} - l_o(\dot{\theta} + \dot{\beta} - \Omega)\sin\beta]\boldsymbol{c}_1 \\ & + [R_{\text{cm}}(\dot{\theta} - \Omega) + l_o(\dot{\theta} + \dot{\beta} - \Omega)\cos\beta]\boldsymbol{c}_2\end{aligned} \tag{20}$$

For calculating the aerodynamic forces the area of the tether is broken into segments and lumped to the nodes. The drag force acting at the ith node can be represented as

$$\boldsymbol{F}_{\text{di}} = -\tfrac{1}{2}\rho_i C_{\text{dt}} S_i V_i \boldsymbol{V}_i \tag{21}$$

The velocity of the ith node relative to the atmosphere is written as

$$\begin{aligned}\boldsymbol{V}_i = {} & [\dot{R}_{\text{cm}} - f(l_i)(\dot{\theta} + \dot{\beta} - \Omega)\sin\beta]\boldsymbol{c}_1 \\ & + [R_{\text{cm}}(\dot{\theta} - \Omega) + f(l_i)(\dot{\theta} + \dot{\beta} - \Omega)\cos\beta]\boldsymbol{c}_2\end{aligned} \tag{22}$$

where $f(l_i)$ is determined from Eq. (10). The total force acting on the tether $\boldsymbol{F}_{\text{dt}}$ is determined from the sum of the contributions of the individual nodes.

The moment generated by the atmospheric drag force acting on the orbiter is calculated using

$$\begin{aligned}\boldsymbol{M}_{\text{do}} = (\boldsymbol{R}_o - \boldsymbol{R}_{\text{cm}}) \times \boldsymbol{F}_{\text{do}} = {} & -\tfrac{1}{2}\rho_o C_{\text{do}} S_o l_o V_o \\ & \times [R_{\text{cm}}(\dot{\theta} - \Omega)\cos\beta - \dot{R}_{\text{cm}}\sin\beta + l_o(\dot{\theta} + \dot{\beta} - \Omega)]\boldsymbol{c}_3\end{aligned} \tag{23}$$

Adding the contributions of individual nodes gives the total moment generated by drag forces acting on the tether, which is defined as

$$\begin{aligned}\boldsymbol{M}_{\text{dt}} = \sum (\boldsymbol{R}_i - \boldsymbol{R}_{\text{cm}}) \times \boldsymbol{F}_{\text{di}} = {} & \sum -\frac{1}{2}\rho_i C_{\text{di}} S_i f(l_i) V_i \\ & \times [R_{\text{cm}}(\dot{\theta} - \Omega)\cos\beta - \dot{R}_{\text{cm}}\sin\beta + f(l_i)(\dot{\theta} + \dot{\beta} - \Omega)]\boldsymbol{c}_3\end{aligned} \tag{24}$$

Atmospheric Probe Aerodynamic Forces

As discussed earlier, the TSS-AGA concept implements an aerodynamic lifting surface tethered to a primary mass. Subsequently, the probe is modeled as a wedge, which is capable of generating lift and drag forces depending upon its angle of attack. A Newtonian model of hypersonic flow is adopted to determine the pressure acting on the surface of the wedge. By this approach the pressure coefficient for a surface deflecting the freestream flow is modeled as[28]

$$C_p = \begin{cases} 2\sin^2\delta, & \delta \geq 0 \\ 0, & \delta < 0 \end{cases} \tag{25}$$

Figure 4 shows the profile of the wedge and its relevant geometry. For a particular angle of attack α and wedge angle γ, the flow-deflection angle is determined from

$$\delta_l = \alpha + \gamma/2 \tag{26}$$

$$\delta_u = -\alpha + \gamma/2 \tag{27}$$

where δ_l and δ_u correspond to the deflections at the upper and lower surfaces, respectively. The pressure P on a wedge surface can be determined from C_p, which is defined as

$$C_p = (P - P_\infty) \big/ \left(\tfrac{1}{2}\rho_\infty V_p^2\right) \tag{28}$$

In this equation P_∞ and ρ_∞ denote the freestream conditions at the altitude of the probe. The velocity of the probe relative to the atmosphere can be written as

$$\begin{aligned}\boldsymbol{V}_p = {} & [\dot{R}_{\text{cm}} + l_p(\dot{\theta} + \dot{\beta} - \Omega)\sin\beta]\boldsymbol{c}_1 \\ & + [R_{\text{cm}}(\dot{\theta} - \Omega) - l_p(\dot{\theta} + \dot{\beta} - \Omega)\cos\beta]\boldsymbol{c}_2\end{aligned} \tag{29}$$

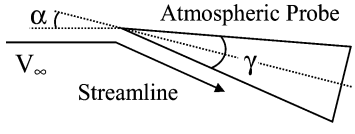

Fig. 4 Atmospheric probe geometry and freestream deflection.

The drag and lift forces acting on the probe are

$$\boldsymbol{F}_{\mathrm{dp}} = \sum_{j=u,l} [PA \sin\delta_j(-\boldsymbol{V}_p \cdot \boldsymbol{c}_1)/V_p \boldsymbol{c}_1 + PA \sin\delta_j(-\boldsymbol{V}_p \cdot \boldsymbol{c}_2)/V_p \boldsymbol{c}_2] \tag{30}$$

$$\boldsymbol{F}_{\mathrm{lp}} = \sum_{j=u,l} [\psi PA \cos\delta_j(-\boldsymbol{V}_p \cdot \boldsymbol{c}_2)/V_p \boldsymbol{c}_1 - \psi PA \cos\delta_j(-\boldsymbol{V}_p \cdot \boldsymbol{c}_1)/V_p \boldsymbol{c}_2] \tag{31}$$

where j denotes the contribution of the upper and lower surface of the wedge. The term ψ is defined as

$$\psi = \begin{cases} 1, & -\boldsymbol{V}_p \cdot \boldsymbol{c}_2 \le 0 \\ 1, & -\boldsymbol{V}_p \cdot \boldsymbol{c}_2 > 0 \end{cases} \tag{32}$$

Orienting the probe during the system's flight through the atmosphere presents a challenging control problem, which is beyond the scope of this work. Therefore, a constant angle of attack is assumed for the probe during the system's interaction with the atmosphere. Finally, the respective moments generated by the lift and drag forces acting on the probe can be written as

$$\boldsymbol{M}_{\mathrm{dp}} = (\boldsymbol{R}_p - \boldsymbol{R}_{\mathrm{cm}}) \times \boldsymbol{F}_{\mathrm{dp}} = (-\boldsymbol{F}_{\mathrm{dp}} \cdot \boldsymbol{c}_2 l_p \cos\beta + \boldsymbol{F}_{\mathrm{dp}} \cdot \boldsymbol{c}_1 l_p \sin\beta)\boldsymbol{c}_3 \tag{33}$$

$$\boldsymbol{M}_{\mathrm{lp}} = (\boldsymbol{R}_p - \boldsymbol{R}_{\mathrm{cm}}) \times \boldsymbol{F}_{\mathrm{lp}} = (-\boldsymbol{F}_{\mathrm{lp}} \cdot \boldsymbol{c}_2 l_p \cos\beta + \boldsymbol{F}_{\mathrm{lp}} \cdot \boldsymbol{c}_1 l_p \sin\beta)\boldsymbol{c}_3 \tag{34}$$

Equations of Motion

The assembled equations of motion of the system are

$$m\left(\ddot{R}_{\mathrm{cm}} - R_{\mathrm{cm}}\dot{\theta}^2\right) = (\boldsymbol{F}_{\mathrm{go}} + \boldsymbol{F}_{\mathrm{gp}} + \boldsymbol{F}_{\mathrm{gt}} + \boldsymbol{F}_{\mathrm{do}} + \boldsymbol{F}_{\mathrm{dt}} + \boldsymbol{F}_{\mathrm{dp}} + \boldsymbol{F}_{\mathrm{lp}}) \cdot \boldsymbol{c}_1 \tag{35}$$

$$m(R_{\mathrm{cm}}\ddot{\theta} + 2\dot{R}_{\mathrm{cm}}\dot{\theta}) = (\boldsymbol{F}_{\mathrm{go}} + \boldsymbol{F}_{\mathrm{gp}} + \boldsymbol{F}_{\mathrm{gt}} + \boldsymbol{F}_{\mathrm{do}} + \boldsymbol{F}_{\mathrm{dt}} + \boldsymbol{F}_{\mathrm{dp}} + \boldsymbol{F}_{\mathrm{lp}}) \cdot \boldsymbol{c}_2 \tag{36}$$

$$\left[m_p l_p^2 + m_o l_o^2 + m_t/(3l)\left(l_o^3 + l_p^3\right)\right](\ddot{\beta} + \ddot{\theta}) = (\boldsymbol{M}_{\mathrm{go}} + \boldsymbol{M}_{\mathrm{gp}} + \boldsymbol{M}_{\mathrm{gt}} + \boldsymbol{M}_{\mathrm{do}} + \boldsymbol{M}_{\mathrm{dt}} + \boldsymbol{M}_{\mathrm{dp}} + \boldsymbol{M}_{\mathrm{lp}}) \cdot \boldsymbol{c}_3 \tag{37}$$

where m is defined as

$$m = m_o + m_p + m_t \tag{38}$$

Numerical Results

Two mission types are considered in the current research. The first, case 1, involves a flyby of Mars in which the tethered system remains unchanged. In case 2, however, the system mass is separated resulting in the orbiter and probe reaching two different final destinations. All simulations begin at a radius equal to that of the Martian sphere-of-influence (SOI). In addition, the simulations are terminated once the SOI is reached after the point of closest approach. The hyperbolic trajectory of the system undergoing the aerogravity-assist maneuver is determined based upon a specified hyperbolic excess speed and a target periapse radius for the system center of mass (CM). The equations of motion for the tethered system are propagated in MATLAB® using an inbuilt Runga–Kutta solver.

Some of the key properties of the orbiter-tether-probe system common to all the numerical simulations are presented in Table 1. The wedge angle is specified to be 10 deg to approximate an ideal hypersonic lifting surface. It is important to note that the system is initially rotating to ensure that tension is maintained in the tether during the uncontrolled flyby. The corresponding velocity of the probe, relative to the system's center of mass, for this rotation is approximately 258 m/s. As reported in Table 1, the tether diameter is only 1 mm. A small diameter reduces the drag acting on the tether and the mass of the system. Minimizing the drag is important for the accuracy of the rigid-rod approximation. Significant normal forces can result in deformation of the tether, which requires analysis with a flexible system model. The number of nodes selected is somewhat arbitrary, but running the simulations with 31 tether nodes (Table 1) ensures that there is less than 1% error between the mass moment of inertia determined using the nodal representation and the value determined by treating the tether as a thin rod.

Table 1 Common simulation properties

Property	Value
Orbiter mass m_o	1600 kg
Probe mass m_p	800 kg
Tether mass m_t	137 kg
Tether length	180 km
Tether diameter	1 mm
Orbiter drag coefficient C_{do}	2
Tether drag coefficient C_{dt}	2
Probe length	7.88 m
Probe width	4 m
Wedge angle γ	10 deg
Orbiter frontal surface area	10 m^2
Initial rotation rate $\dot{\alpha}$	−0.0022 rad/s
Initial orbit radius	577,000 km
Number of tether nodes	31

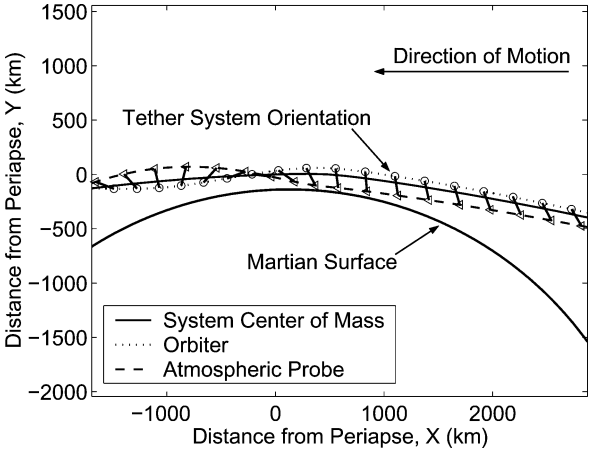

Fig. 5 System trajectory and tether orientation near periapse for case 1 (initial V_∞ = 8 km/s, target periapse altitude = 160 km).

Case 1

To augment the gravity assist provided by Mars, the rotating tethered satellite system is permitted to interact with the Martian atmosphere. In this scenario, which is referred to as an intact-system maneuver, the physical properties of the system remain constant throughout the flyby. A typical flight path of the system near periapse is shown in Fig. 5. The behavior of the system corresponds to a simulation with an initial hyperbolic excess speed of 8 km/s, a target periapse altitude for the CM of 160 km, and a probe angle of attack of −15 deg. It can be seen in Fig. 5 that the tether remains rigid during the maneuver and that its length does not change. The initial orientation of the system is selected to guarantee that a near-vertical orientation at periapse is achieved. This orientation also ensures that the probe reaches a lower altitude than the orbiter. Inspection of the results reveals that a minimum probe altitude of 42 km is achieved while the orbiter drops to an altitude of 147 km. The minimum orbiter altitude is not an ideal result, but this configuration emphasizes the transition from negative to positive rotation of the system due to aerodynamic forces. Figure 6 illustrates the change in rotation between the pre- and postflyby states in more detail.

The range of design variables in the intact-system maneuver is inherently enormous. For a tethered system performing an aerogravity-assist maneuver, it is possible to change the system's

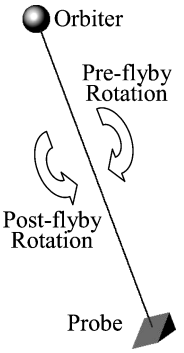

Fig. 6 Pre- and postflyby rotations.

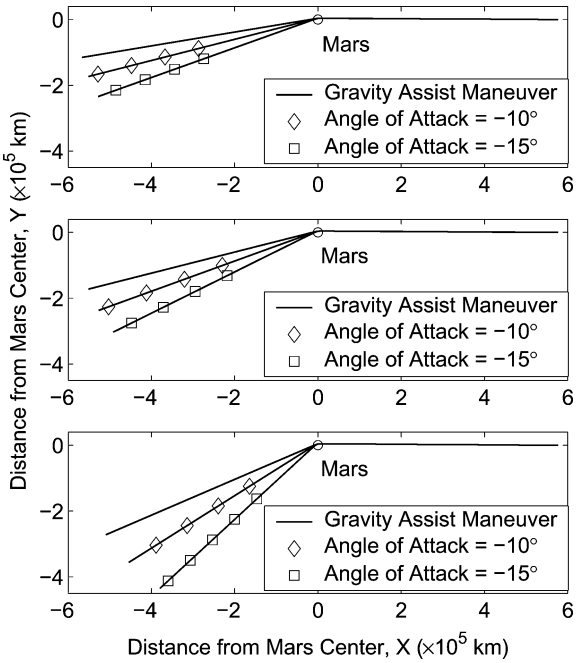

Fig. 7 System trajectories for aerogravity-assist maneuvers (case 1).

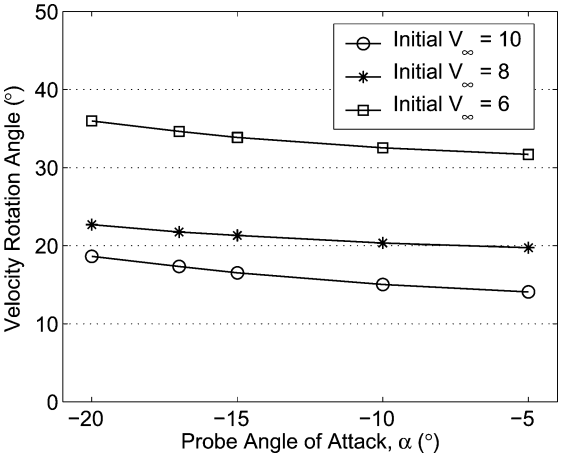

Fig. 8 Rotation angle of velocity vector (relative to the planet) vs probe angle of attack for case 1.

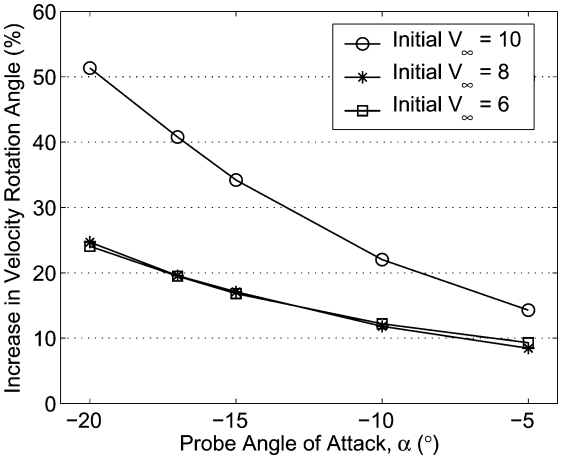

Fig. 9 Percentage increase in rotation angle of the velocity (relative to the planet) from rotation achieved through a GA maneuver for case 1.

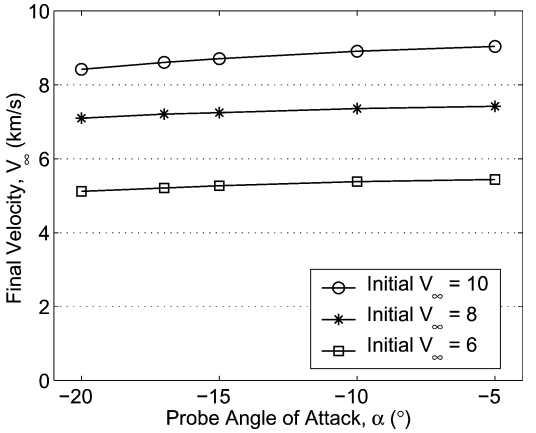

Fig. 10 Final hyperbolic excess speed vs probe angle of attack (case 1).

initial rotation rate and orientation, as well as the system's many physical properties. In addition, trajectory parameters such as hyperbolic excess speed and target periapse radius can be varied. The number of design choices pose a challenging optimization problem. The goal of optimizing the flybys would be to maximize the change in heliocentric velocity while minimizing the forces acting on the system and the aerodynamic heating. The intact-system maneuvers reported in this paper are not optimized but rather selected as examples from a search space of over 2800 different configurations. The reported flyby scenarios are chosen as they demonstrate significant increases in the change of the system's heliocentric velocity relative to a traditional gravity-assist (GA) maneuver. Also, the reported scenarios maintain the orbiter above an altitude of 200 km. The target periapse for the flybys reported in Figs. 7–12 is 165 km, which is selected as reasonable compromise between the resulting velocity deflection and force loads. Each of the initial hyperbolic excess speeds considered require different initial tether orientations to ensure the system achieves a near-vertical orientation at periapse. The simulations of the flybys are very sensitive to the initial system orientation and rotation rate as they affect the depth, speed, and duration of the system's interaction with the atmosphere.

Figure 7 shows the system trajectories for three approach velocities and two different probe angles of attack. For comparison, trajectories of the system undergoing a gravity-assist maneuver are included in the plots. The GA trajectory is developed using a simulation equivalent to the AGA maneuver except that the atmospheric forces are neglected. Significant deflections of the system trajectory relative to the GA maneuver are clearly shown in Fig. 7. The maximum deflections for the simulations with initial hyperbolic excess speeds of 10, 8, and 6 km/s are 18.6, 22.7, and 36.0 deg, respectively. As expected, Fig. 8 reveals that larger angles of attack and lower initial speeds produce greater deflections of the tethered system's velocity. Figure 9 shows the percentage increase in the deflection of the velocity vector (relative to the planet) with respect to the deflection achieved by the GA maneuver. For a probe angle of attack of −20 deg, the velocity deflections represent increases of between 22 and 52%. The percentage grows dramatically as the magnitude of the probe's angle of attack is increased for the scenario with an initial hyperbolic excess speed of 10 km/s. To generate these deflections,

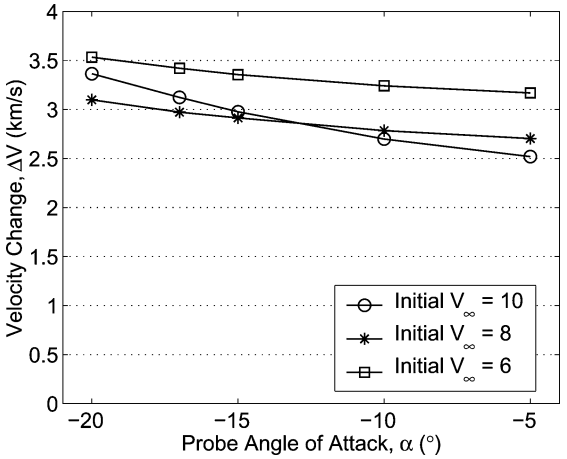

Fig. 11 Total change in heliocentric velocity of the spacecraft vs probe angle of attack (case 1).

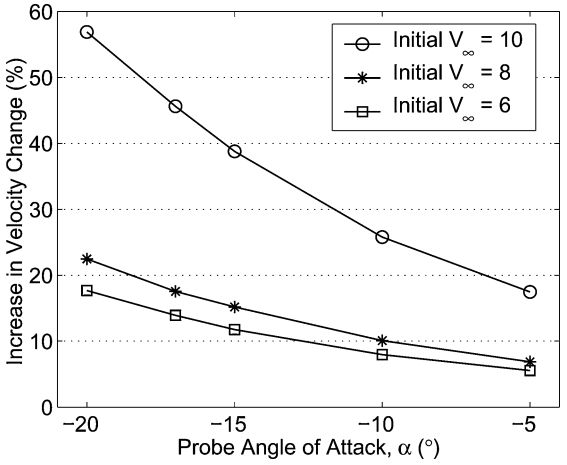

Fig. 12 Percentage increase in the magnitude of the heliocentric velocity change from the velocity change achieved through a GA maneuver (case 1).

however, high aerodynamic loads are applied to the system with notable losses in hyperbolic excess speed. Figure 10 displays the hyperbolic excess speeds of the system as it leaves the SOI of Mars for a range of initial speeds and probe orientations. As the magnitude of the probe's angle of attack increases, so does the loss in the final speed and the velocity deflection angle. From Fig. 10 it can be seen that the maximum speed loss is about 1.58 km/s with a probe angle of attack of −20 deg and an initial hyperbolic excess speed of 10 km/s. The total change in the heliocentric velocity, shown in Fig. 11, is determined from the geometry of the initial and final heliocentric velocity vectors and, therefore, includes the velocity rotation and loss in speed. For the presented configurations the total change in heliocentric velocity ranges from 2.5 to about 3.5 km/s. The scenario with an initial hyperbolic excess speed of 10 km/s shows a faster growth in the magnitude of the heliocentric velocity change, with respect to the probe's angle of attack, than the other scenarios. Figure 12 presents the percentage increase in the heliocentric velocity change relative to what can be achieved with a GA maneuver. The respective maximum increases for the scenarios with initial speeds of 10, 8, and 6 km/s are 57.0, 22.5, and 17.7%. Again, the scenario with an initial speed of 10 km/s produces the greatest percentage increases.

Significant force loads affect the tethered satellite system as it interacts with the atmosphere of Mars. Figure 13 presents the maximum forces calculated at the attachment points between the tether and the end masses. As shown in Fig. 14, axial forces act in the direction of an axis collinear with the length of the tether. The positive axial forces determined at the attachment point between the

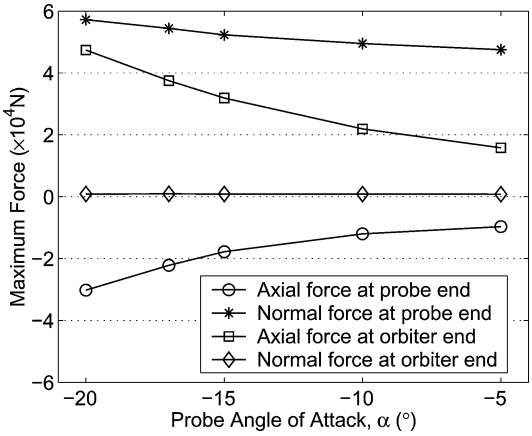

Fig. 13 Maximum force produced during intact system flybys with an initial V_∞ of 10 km/s.

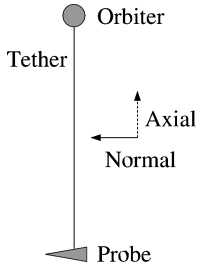

Fig. 14 Direction of positive forces acting on the tether ends induced by the end masses.

tether and the orbiter indicate that the orbiter is pulling away from the tether in the axial direction. Similarly, the negative axial forces calculated at the attachment point between the tether and the probe indicate that the probe is pulling away from the tether in the axial direction. As both the orbiter and probe are pulling away from the attachment points, the tether is in tension when the axial forces reach a maximum. From Fig. 14 it can be seen that positive normal forces act on the tether attachment points normal to the tether length. The maximum normal forces are positive at both attachment points, indicating that the end masses are pulling the tether forward in the direction of the positive normal force. At the attachment point between the orbiter and the tether, the maximum normal forces are relatively small and do not change significantly with respect to the probes angle of attack. However, the maximum normal forces predicted at the interface between the tether and the probe are large as a result of a difference between the ballistic coefficients of the tether and the probe. The difference between the ballistic coefficients causes the tether to retard the motion of the probe through the atmosphere. More closely matching the ballistic coefficients of the tether and probe (aeromatching[19]) can alleviate the magnitude of the normal force. In general, the magnitudes of the forces generated at the tether ends are dependent on the altitude, velocity, and orientation of the tether during the flyby.

The high forces, which are acting on a tether with a 1 mm diam, are in excess of the strength limits of commonly modeled materials. One candidate material, Spectra 2000, has a tensile strength as high as 3.5 GPa (data available online at http://www.spectrafiber.com/products/spectra_2000.html [cited 11 March 2003]). Implementing a tether with a larger diameter enables the system to withstand these loads, but will increase the magnitude of the atmospheric drag forces and the mass of the tether. As the tether is actually a flexible body, it is reasonable to assume that the loads act in tension only. If the forces act on a tether axially, employing a diameter of 2 mm produces maximum loads tolerable by Spectra 2000 for flybys with an initial hyperbolic excess speed of 6 km/s. Similarly, a diameter of 2.5 mm will produce tolerable loads for flybys with an initial hyperbolic excess speed of 8 km/s. The cost, in terms of mass, is quite significant with tether diameters of 1, 2, and 2.5 mm corresponding to masses of 137, 549, and 857 kg, respectively. A material with a higher strength-to-weight ratio would

be the preferable method for accommodating the high loads. Developing materials, such as carbon nanotubes, are expected to be capable of withstanding the loads demonstrated in a tether with a small diameter.[29] For near-term applications more conservative flyby scenarios will need to be adopted in order to minimize the loads and the tether mass.

Case 2

Using a tethered satellite system to deliver two mission packages to different destinations presents some interesting possibilities for interplanetary exploration. In this investigation the probe and orbiter are released from the tether near periapse while the system is undergoing an aerogravity-assist maneuver. Separation results in the two masses following independent trajectories. The reported results show that the dual-destination mission scenario is quite promising for delivering payloads to different destinations. For comparison, the system configurations adopted for the reported dual-destination missions are the same as the intact-system maneuvers. Table 2 lists the results obtained for three initial hyperbolic excess speeds. The results represent the highest target periapse altitude at which the probe is able to land on the planet's surface. Solutions at lower altitudes are possible at the cost of larger forces acting on the system and lower minimum altitudes for the orbiter. The simulations of the dual-destination mission reveal that the final orbiter conditions are not dependent on the probe's angle of attack when the masses are released from the closest approach point of the probe. Releasing 10 or more seconds after the probe's closest approach point produces greater rotation of the orbiter's velocity. The cost of the increased rotation is higher force magnitudes and failure of the probe to land on the surface. Unlike the other cases, the flyby with an initial hyperbolic excess speed of 8 km/s requires a lower target periapse to enable the probe to land on the surface of Mars.

The behavior of the dual-destination mission scenario is clearly illustrated in Fig. 15. This graph depicts the altitude of the orbiter, probe, and system center of mass near the periapse of the hyperbolic flyby trajectory. In the figure it is possible to observe that the end masses are released at the closest approach point of the probe, which enables the end masses to follow independent trajectories. For reference, the trajectory of the intact system is also represented in Fig. 15. The results are for a hyperbolic orbit with a periapse altitude of 150 km and a hyperbolic excess speed of 8 km/s. The probe is assumed to maintain an angle of attack of −10 deg until release. Once released from the system, the angle of attack is decreased in order to increase drag. The final destination for the probe is the surface of Mars. For the orbiter, however, the journey continues with a postflyby velocity that is deflected by 21.1 deg from the initial velocity of the system.

Table 2 Simulated dual-destination missions (case 2)

Hyperbolic excess speed	10	8	6
Target periapse altitude for the system CM, km	160	150	160
Wedge angle of attack, deg	−10	−10	−10
Total velocity deflection of the orbiter by the dual-destination maneuver, deg	13.8	21.1	30.9
Final speed, km/s	9.55	7.48	5.60
Total heliocentric velocity change, km/s	2.39	2.88	3.11
Minimum altitude reached by the orbiter, km	220	205	225
Potential velocity deflection by a GA maneuver with 200-km periapse altitude, deg	12.2	18.0	28.8
Percentage increase in heliocentric velocity change relative to GA maneuver, %	12	15	4

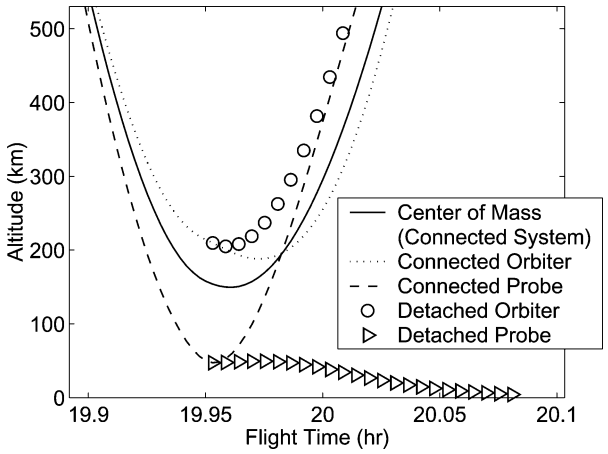

Fig. 15 System altitude vs flight time near periapse for case 2 (initial V_∞ = 8 km/s, target periapse altitude = 150 km).

For the dual-destination mission depicted in Fig. 15, the postflyby trajectory of the system undergoing an intact-system maneuver is rotated more than that of the detached orbiter for the same flight conditions. The larger deflection, however, is associated with a significant decrease in the hyperbolic excess speed of the system and results in the orbiter dropping below 200 km. The final speed of the intact system represented in Fig. 15 is 6.4 km/s, which represents a loss of 1.6 km/s. For the detached orbiter the final speed is 7.5 km/s, which corresponds to a loss of only 0.5 km/s. A total change of 2.9 km/s in the orbiter's heliocentric velocity is determined from the geometry of the pre- and postflyby velocities. The increase in the total heliocentric velocity change of the orbiter compared to performing a GA maneuver with a target periapse of 200 km is around 15%. For the cases with initial hyperbolic excess speeds of 10 and 6 km/s, the changes in heliocentric velocity are 2.39 and 3.11 km/s, respectively. As shown in Table 2, these velocity changes represent increases of 12 and 4% relative to the corresponding GA maneuvers with periapse altitudes of 200 km. The example flyby scenarios indicate that the dual-destination mission generates significant changes in the heliocentric velocity of the orbiter and permits the probe to land on the planet's surface.

Conclusions

Two mission cases for the tethered satellite system-aerogravity-assist concept are investigated using ambitious mission scenarios. The simulation results indicate that these mission types are effective in producing significant changes in velocity without the use of propellant. In addition, it is shown that each mission case is capable of maintaining part of the system mass outside of the sensible atmosphere. Modeling the behavior of a flexible tether system during an aerogravity-assist maneuver, developing appropriate control strategies, and, ultimately, optimizing the mission configuration are identified as important design challenges. Depending on the parameters of the mission and the available tether materials, the tethered satellite system-aerogravity-assist concept might be practical for future space exploration.

References

[1]van der Heide, E. J., Carroll, J. A., and Kruijff, M., "Options for Coordinated Multi-Point Sensing in the Lower Thermosphere," *Physics and Chemistry of the Earth, Part C: Solar, Terrestrial and Planetary Science*, Vol. 26, No. 4, 2001, pp. 285–291.

[2]Pasca, M., and Lorenzini, E., "Collection of Martian Atmospheric Dust with a Low Altitude Tethered Probe," *Advances in the Astronautical Sciences*, Vol. 75, 1991, pp. 1121–1139.

[3]Pasca, M., and Lorenzini Enrico, C., "Optimization of a Low Altitude Tethered Probe for Martian Atmospheric Dust Collection," *Journal of the Astronautical Sciences*, Vol. 44, No. 2, 1996, pp. 191–205.

[4]Anderson, J. L., "Space-Tethered Atmospheric Systems," *Journal of the British Interplanetary Society*, Vol. 44, No. 3, 1991, pp. 103–110.

[5]Bogar, T. J., Bangham, M. E., Forward, R. L., and Lewis, M. J., "Hypersonic Airplane Space Tether Orbital Launch (HASTOL) System: Interim Study Results," AIAA Paper 99-4802, Nov. 1999.

[6]Longuski, J. M., and Puig-Suari, J., "Hyperbolic Aerocapture and Elliptic Orbit Transfer with Tethers," International Astronautical Federation, Paper 91-339, Oct. 1991.

[7]Kim, E., and Vadali, S. R., "Nonlinear Feedback Deployment and Retrieval of Tethered Satellite Systems," *Journal of Guidance, Control, and Dynamics*, Vol. 15, No. 1, 1992, pp. 28–34.

[8]Breakwell, J. V., and Gearhart, J. W., "Pumping a Tethered Configuration to Boost Its Orbit Around an Oblate Planet," *Journal of Astronautical Sciences*, Vol. 35, No. 1, 1987, pp. 19–39.

[9]Kokubun, K., and Fujii, H. A., "Deployment/Retrieval Control of a Tethered Subsatellite Under Effect of Tether Elasticity," *Journal of Guidance, Control, and Dynamics*, Vol. 19, No. 1, 1996, pp. 84–90.

[10]Keshmiri, M., Misra, A. K., and Modi, V. J., "General Formulation for N-Body Tethered Satellite System Dynamics," *Journal of Guidance, Control, and Dynamics*, Vol. 19, No. 1, 1996, pp. 75–83.

[11]Bainum, P. M., Diarra, C. M., and Kumar, V. K., "Shuttle-Tethered Subsatellite System Stability with a Flexible Massive Tether," *Journal of Guidance, Control, and Dynamics*, Vol. 8, No. 2, 1985, pp. 230–234.

[12]Kim, E., and Vadali, S. R., "Modeling Issues Related to Retrieval of Flexible Tethered Satellite Systems," *Journal of Guidance, Control, and Dynamics*, Vol. 18, No. 5, 1995, pp. 1169–1176.

[13]Biswell, B. L., Puig-Suari, J., Longuski, J. M., and Tragesser, S. G., "Three-Dimensional Hinged-Rod Model for Elastic Aerobraking Tethers," *Journal of Guidance, Control, and Dynamics*, Vol. 21, No. 2, 1998, pp. 286–295.

[14]No, T. S., and Cochran, J. E., Jr., "Dynamics and Control of a Tethered Flight Vehicle," *Journal of Guidance, Control, and Dynamics*, Vol. 18, No. 1, 1995, pp. 66–72.

[15]No, T. S., and Cochran, J. E., Jr, "Dynamics and Stability Analysis of an Orbiter-Tether-Maneuverable Subsatellite System," American Astronautical Society, Paper AAS-91-172, Feb. 1991.

[16]Bae, G., Sim, E., and Barlow, J. B., "Atmospheric Flight Equations of a Tethered Hypersonic Waverider," *Advances in the Astronautical Sciences*, Vol. 82, Feb. 1993, pp. 1283–1296.

[17]Biswell, B., and Puig-Suari, J., "Stability and Control of an Atmospheric Tether with a Lifting Probe," *Journal of Guidance, Control, and Dynamics*, Vol. 22, No. 5, 1999, pp. 664–670.

[18]Warnock, T. W., and Cochran, J. E., Jr., "Predicting the Orbital Lifetime of Tethered Satellite Systems," *Acta Astronautica*, Vol. 35, No. 2–3, 1995, pp. 193–203.

[19]Longuski, J. M., Puig-Suari, J., and Mechalas, J., "Aerobraking Tethers for the Exploration of the Solar System," *Acta Astronautica*, Vol. 35, No. 2–3, 1995, pp. 205–214.

[20]Tragesser, S. G., Longuski, J. M., and Puig-Suari, J., "Global Minimum Mass for Aerobraking Tethers," *Journal of Guidance, Control, and Dynamics*, Vol. 20, No. 6, 1997, pp. 1260–1262.

[21]Biswell, B. L., "Active Control of an Atmospheric Tether Using a Lifting Probe," Ph.D. Dissertation, Dept. of Mechanical and Aerospace Engineering, Arizona State Univ., Tempe, AZ, Dec. 1998.

[22]Lohar, F. A., Misra, A. K., and Mateescu, D., "Optimal Atmospheric Trajectory for Aerogravity Assist with Heat Constraint," *Journal of Guidance, Control, and Dynamics*, Vol. 18, No. 4, 1995, pp. 723–730.

[23]Lohar, F. A., Misra, A. K., and Mateescu, D., "Mars–Jupiter Aerogravity Assist Trajectories for High-Energy Missions," *Journal of Spacecraft and Rockets*, Vol. 34, No. 1, 1997, pp. 16–21.

[24]Sims, J. A., Longuski, J. M., and Patel, M. R., "Aerogravity-Assist Trajectories to the Outer Planets and the Effect of Drag," *Journal of Spacecraft and Rockets*, Vol. 37, No. 1, 2000, pp. 49–55.

[25]Randolph, J. E., and McRonald, A. D., "Solar System 'Fast Mission' Trajectories Using Aerogravity Assist," *Journal of Spacecraft and Rockets*, Vol. 29, No. 2, 1992, pp. 223–232.

[26]McRonald, A. D., and Randolph, J. E., "Hypersonic Maneuvering for Augmenting Planetary Gravity Assist," *Journal of Spacecraft and Rockets*, Vol. 29, No. 2, 1992, pp. 216–222.

[27]Thomson, W. T., *Introduction to Space Dynamics*, Wiley, New York, 1961, pp. 14–16, 102–104.

[28]Anderson, J. D., Jr., *Hypersonic and High Temperature Gas Dynamics*, McGraw–Hill, New York, 1989, pp. 46–53.

[29]Smitherman, D. V., Jr., "Space Elevators: An Advanced Earth–Space Infrastructure for the New Millennium," NASA CP-2000-210429, Aug. 2000.

D. B. Spencer
Associate Editor